

Highly Compressible Integrated Supercapacitor–Piezoresistance-Sensor System with CNT–PDMS Sponge for Health Monitoring

Yu Song, Haotian Chen, Zongming Su, Xuexian Chen, Liming Miao, Jinxin Zhang, Xiaoliang Cheng, and Haixia Zhang*

Rapid improvement of wearable electronics stimulates the demands for the matched functional devices and energy storage devices. Meanwhile, wearable microsystem requires every parts possessing high compressibility to accommodate large-scale mechanical deformations and complex conditions. In this work, a general carbon nanotube–polydimethylsiloxane (CNT–PDMS) sponge electrode is fabricated as the elementary component of the compressible system. CNT–PDMS sponge performs high sensitivity as a piezoresistance sensor, which is capable of detecting stress repeatedly and owns great electrochemical performance as a compressible supercapacitor which maintains stably under compressive strains, respectively. Assembled with the piezoresistance sensor and the compressible supercapacitor, such highly compressible integrated system can power and modulate the low-power electronic devices reliably. More importantly, attached to the epidermal skin or clothes, it can detect human motions, ranging from speech recognition to breathing record, thus showing feasibility in real-time health monitor and human–machine interfaces.

1. Introduction

With the development of the elastic electronics^[1] and wearable devices,^[2] researchers are conducting every efforts to pursue the matched power units^[3,4] and functional devices.^[5,6] Due to the widespread applications, wearable devices are usually required to be integrated into nonplanar substrates

and confined into a limited area, therefore, the ability to tolerate large strains without remarkable loss in their performance is crucial to the whole systems.^[7–10] However, normal functional devices and power units may fail to work stably and be fragile by excessively compressive strains. In addition, the external power supply would increase the complexity of the device and decrease the system integrity. As a result, the highly compressible system with stable functions^[11,12] and integrated configuration^[13,14] are in great demands.

Nowadays, among various sensors to detect human motion and monitor health condition,^[5,15] piezoresistive sensors (PRs), which are typical sensors that transduce the external pressure into the resistance signal, have been widely used in wearable devices due to their advantages of cost-efficient fabrication and simple structure.^[16–18] Normal PRs with conductive polymers or particles are proved suitable sensing materials,^[19–21] but these materials are confronted with low sensitivity and poor stability especially in low-pressure regimes. Different from the conventional PRs, conductive porous sponges or foams have been developed,^[22,23] which are considered as alternative materials owing to their

Y. Song, Z. Su, L. Miao, J. Zhang, X. Cheng,
Prof. H. Zhang
National Key Lab of Nano/Micro Fabrication
Technology
Institute of Microelectronics
Peking University
Beijing 100871, China
E-mail: zhang-alice@pku.edu.cn

H. Chen, X. Chen, Prof. H. Zhang
Academy for Advanced Interdisciplinary Studies
Peking University
Beijing 100871, China

DOI: 10.1002/sml.201702091



synergistic effect of high conductivity of active materials and excellent mechanical property of porous scaffold. Employed with chemical vapor deposition^[24] or carbonization process,^[25] sponge-like material-based PRS performs high sensitivity and low strain detecting capability, satisfying the demands of wearable applications.^[26,27] However, the aforementioned PRS has several problems, such as low integration, complex fabrication, and expensive materials (graphene, silver/gold nanowires, or nanoparticles, etc.).

Additionally, in order to power wearable devices and compose a self-powered compressible system, energy storage devices, which could maintain performance under large strains, should be further discussed.^[28–30] Considering the fact that conventional solid-state supercapacitors composed of carbon-based materials, conducting polymers, and their composites are lack of compressibility,^[31–33] thus the appearance of the advanced supercapacitors called compressible supercapacitors (CSCs) paves the way for practical applications with long cycle life, great stability, and compatibility.^[34,35] The sponge-like structure with high porosity is a remarkable configuration for CSC electrode, such as 3D graphene, aerogel, and carbon nanotubes (CNTs).^[36–38] Unfortunately, this pristine porous structure still has some drawbacks. Due to the relatively poor mechanical property, it tends to collapse under the large compressive stress,^[39] meanwhile, some carbon-based materials are intrinsically hydrophobic, which hinders the infiltration of electrolyte and limits the improvement of the electrochemical performance.^[40] As a result, combination of the high conductivity of filling active materials and great mechanical robustness of the sponge-like scaffold seems to be a considerable attempt for the compressible system.

Therefore, we demonstrate a highly compressible system integrated with PRS and CSC based on the general carbon nanotube–polydimethylsiloxane (CNT–PDMS) sponge which owns both high piezoresistance sensitivity and stable electrochemical performance. On one hand, through simple and low-cost drop-drying process of CNT–PDMS sponge,^[22,41–45] the PRS shows remarkable piezoresistance performance with high sensitivity and wide range of deformations from 26 Pa to more than 60% strains. The resistance response shows quite reliable under repeated stress and reflects both small and large compressive strains accurately. On the other hand, taking advantage of CNT with high conductivity and porous PDMS scaffold with great mechanical robustness,^[22] CNT–PDMS sponge based CSC performs stable electrochemical performance even under large compressive strains (50%). This integrated system owns great compressibility and is able to power and modulate low-power electronic devices. More importantly, such compressible system could be directly attached to the epidermal skin or clothes as the wearable health monitor devices. The PRS shows versatile capabilities in monitoring human motions powered by the charged CSC, such as speech recognition, motion state, and breathing monitoring regardless of the complex working conditions. Therefore, this highly compressible integrated supercapacitor–piezoresistance–sensor system is compliant to widespread applications and shows promising potentials in real-time health monitor.

2. Results and Discussion

As illustrated in **Figure 1a**, this highly compressible integrated wearable system is consisting of two parts: PRS and solid-state CSC. Once the CSC is fully charged, it could be powerful enough to drive the PRS as the real-time monitor with high sensitivity. Such system performs reliably even in large compressible strains, thus broadening the applications of energy storage devices and functional devices. In detail, **Figure 1b** schematically shows the fabrication process of the general compressible CNT–PDMS sponge. By using cube sugars as the pore-creating agent (**Figure 1b (i)**), porous sponge-like PDMS scaffolds (**Figure 1b (ii)**) could be fabricated with high compressibility. The CNT–PDMS sponges with different thickness are then prepared by “drop-drying” strategy based on CNT ink dispersion (**Figure 1b (iii)**). The amount of the CNTs on the PDMS scaffold could be modulated by the “drop-drying” cycles and the concentration of the CNT ink dispersion to meet the demands of different functions, where we utilize CNT–PDMS with low resistance (approximately hundreds of ohms) and high resistance (approximately thousands of ohms) for CSC and PRS, respectively. Scanning electron microscopy (SEM) demonstrates that the PDMS sponges possess an open network of pore with large surface-area, indicating that PDMS completely fills the sugar mold and is capable of being porous materials (**Figure 1c**). With the infiltration of the CNT active materials during drop-drying process, the surface of scaffold becomes rugged in the same scale as shown in **Figure 1d**. Enlarged SEM images of porous CNT–PDMS sponge is demonstrated in **Figure S1** in the Supporting Information, which proves the CNTs are densely coated on the backbone of the PDMS sponge, even in the micrometer-level porous structure. Therefore, the cheap and abundant sugar is essential for the fabrication of the porous CNT–PDMS sponge, which shows suitable candidate as the compressible component in various devices.

2.1. Evaluation of CNT–PDMS Sponge

As mentioned before, by using sugar cubes (**Figure 2a**) as the template, compressible PDMS sponges (**Figure 2b**) are prepared and sectioned into different thicknesses. Then the compressible electrodes could be prepared by filling CNTs as shown in **Figure 2c**. Cube sugars could be purchased with various molds, which results in the corresponding PDMS sponges with any desired shape and size. To quantify the variation of the wettability properties, water contact angle measurements are carried out. The PDMS sponge is in nature hydrophobic with an initial contact angle of 136.1° while with the infiltration of CNT active materials, the CNT–PDMS sponge turns to be highly hydrophilic (33.5°) due to the CNT behavior and the droplet could be completely absorbed within 1 s, as shown in the inset of **Figure 2b,c**. The infiltration of the electrolyte could be greatly enhanced by the hydrophilic characteristic of the CNT–PDMS sponge, which is critical to the improved electrochemical performance.

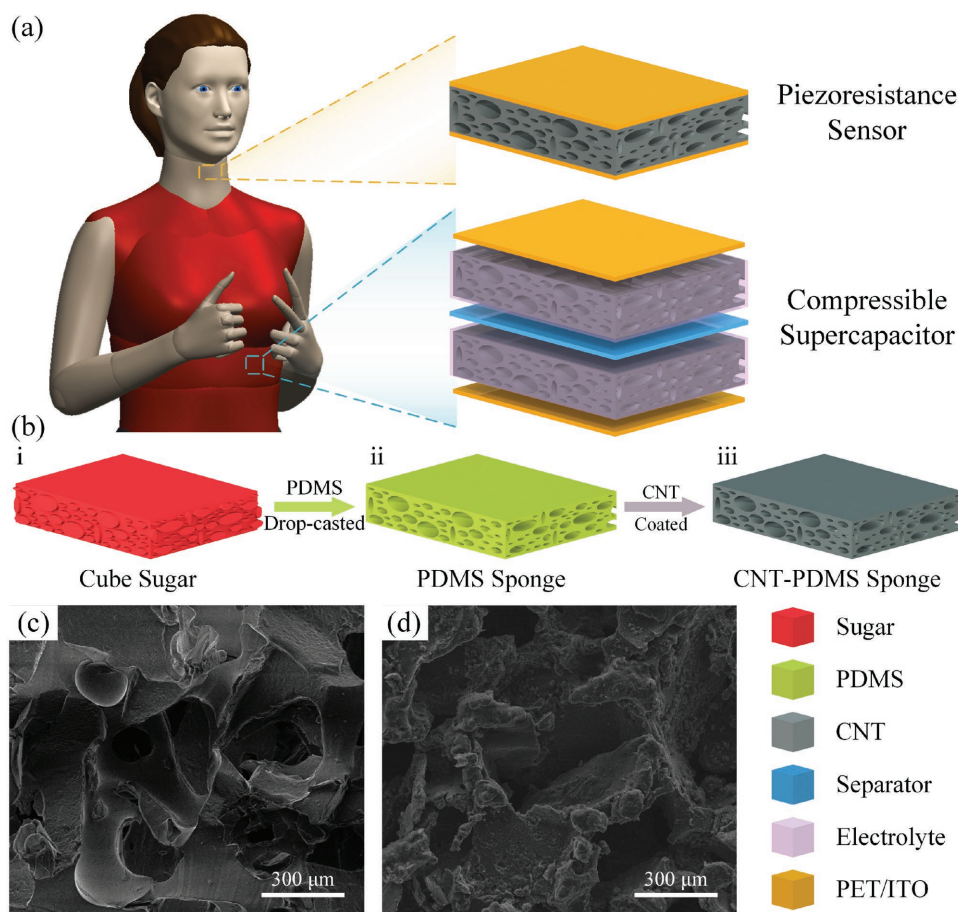


Figure 1. a) Schematic diagram of the highly compressible integrated supercapacitor–piezoresistance-sensor system based on wearable CNT–PDMS sponge. b) Fabrication of the preparing CNT–PDMS sponge. The SEM images of the c) PDMS sponge and d) CNT–PDMS sponge.

Apparently, the concentration of CNT ink and dropping time are two key factors to influence the resistance of the device. Figure 2d demonstrates the relationship of resistance and dropping time under different concentrations of CNT ink. As the dropping time increases, the resistance decreases dramatically until the CNT–PDMS sponge (4 mm) is gradually saturated. Meanwhile, the lower concentration of CNT ink will definitely require longer dropping time to reach the saturation state. In addition, the relative increase of CNT mass on PDMS sponge is correspondingly related to the dropping time and the concentration of the CNT ink as shown in Figure 2e. In order to evaluate the stability of the simple fabrication process, resistances of six CNT–PDMS sponge after 10 dropping times are illustrated in Figure 2f. The average resistance of these samples is 3.51 k Ω and the coefficient of variation is only 2.36%. Furthermore, the thickness of the PDMS sponge also affects the resistance variation along the vertical direction shown in Figure S2 in the Supporting Information.

Figure 2g demonstrates the stress–strain measurements of the prepared CNT–PDMS sponge under different compressive strains, which proves the characteristic behavior of porous sponge-like materials with three distinct stages.^[1,35] At the beginning, when the CNT–PDMS sponge is compressed at $\epsilon < 10\%$, the intact sponge deforms linearly with respect to the stress, which could be described as the elastic region (Region I). This region is followed by a relative

plateau from 10% to 45% (Region II), the stress–strain curve of which exhibits the scaffold is buckled and collapsed. With the stress increasing at $\epsilon > 45\%$ (Region III), the PDMS scaffold with CNTs is crushed together and behaves like bulk materials, showing excellent mechanical performance. While in the releasing process, the releasing curve almost returns to the origin without plastic deformation, indicating that CNT–PDMS sponge could tolerate a large deformation of mechanical strength. In addition, stress–strain measurements with strain of 60% for PDMS sponge and CNT–PDMS sponge are shown in Figure 2h, which perform similar shapes. The CNT–PDMS sponge is more rigid and resistant to compression than the PDMS sponge, which could be explained by the attached CNTs enhancing the mechanical properties. As for CNT–PDMS sponge stability, the resistance is quite steady in the first 200 compressing–releasing process cycles (Figure 2i). Therefore, CNT–PDMS sponge with great mechanical properties and high conductivity could be potentially used in PRS and solid-state CSC, without either an insulating binder or other conducting additive.

2.2. Piezoresistive Properties of PRS

On one hand, with the high compressibility and electronic conductivity, the CNT–PDMS sponge owns capability of

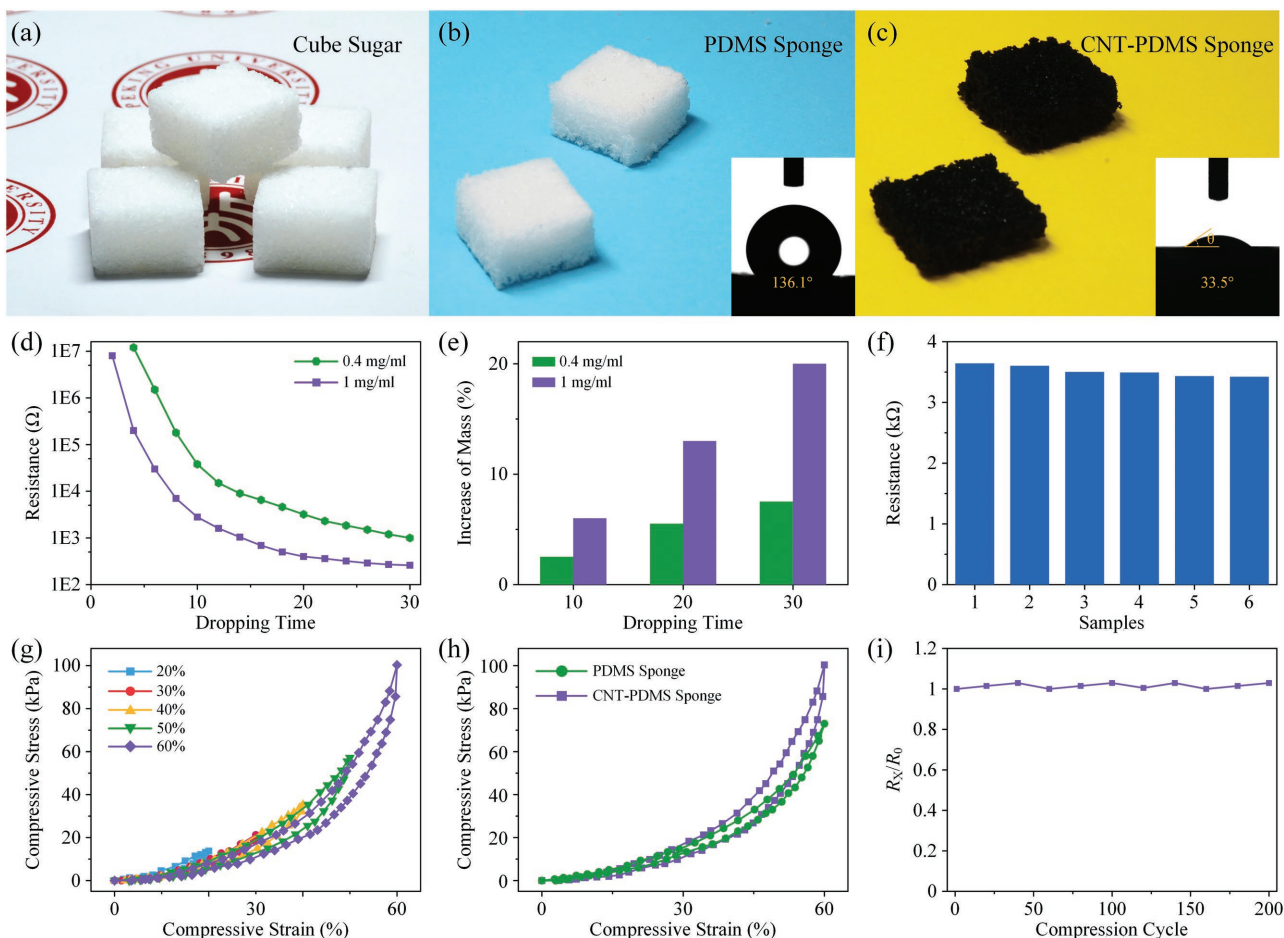


Figure 2. Digital photographs of a) cube sugars, b) PDMS sponge, and c) CNT–PDMS sponge. The inset photographs show the water contact angle of PDMS sponge and CNT–PDMS sponge. The relationship of d) resistance, e) relative increase of CNT mass on PDMS sponge and dropping time with 1 and 0.4 mg mL⁻¹ CNT ink. f) Resistance histogram of six CNT–PDMS sponges after 10 dropping times. g) The compressive stress–strain curves of CNT–PDMS sponge at different strain of 20–60%. h) Compressive stress–strain curves with a maximum strain of 60% for PDMS sponge and CNT–PDMS sponge, respectively. i) Stability of the electrical resistance of CNT–PDMS sponge in the first 200 compressing–releasing cycles.

detecting various strains as well. Particularly, compressive stress mediate the contact area of CNT–PDMS sponge scaffold under different strains (**Figure 3a**), resulting in the conductance modulation. As a result, higher strain leads to larger contact area between CNT–PDMS sponge scaffold and decreases the whole resistance. To further analyze the performance of the PRS, the CNT–PDMS sponge is sandwiched between two PET/ITO electrodes through the push–pull gauge, as shown in **Figure 3b**. The resistance response could be monitored via voltage signal with the stress imposed on the top surface during the compressing process. The resistance response defines $\Delta R/R_0 = (R_0 - R_X)/R_0$, where R_0 and R_X represent the resistance without and with compressive stress, respectively.

To evaluate the relationship of the performance and the resistance of the PRS, three different PRSs have been tested under the same compressive stress. **Figure 3c** indicates that the middle resistance PRS-M (20 k Ω) owns the highest resistance response compared to the PRS-L (70 k Ω) and PRS-S (2 k Ω). It can be proved by the **Figure S3** in the Supporting Information at the same time, where PRS-M also obtains the highest resistance response under the same compressive

strain (10%). The different sensitivity of these PRSs could be explained as follows. As mentioned before, the compressive stress would cause the contact-separation of the CNT–PDMS sponge scaffold and modulate the resistance. For PRS-L, due to the fewer dropping time, the CNTs are incompletely coated among the scaffold, which results the low sensitivity compared to PRS-M and PRS-S with smaller conductive pathways induced by compressive stress. As for PRS-S, considering more CNTs are coated among the scaffold and under the compressive stress, the CNT network is harder to change its structure than PRS-M, which seems relatively insensitive to deformations. Therefore, PRS-M with suitable resistance, which exhibits desirable responses to compressive stress, is employed for the following tests.

First, the current–voltage (I – V) characteristics of PRS under different compressive stress has been studied (**Figure 3d**). It can be seen that PRS displays good linear I – V characteristics under different compressive stress, the slope of which increases with the compressive stress applied owing to the corresponding decrease of resistance. Furthermore, the resistance response of PRS can be directly revealed by the light-emitting diode (LED) test using the PRS as the

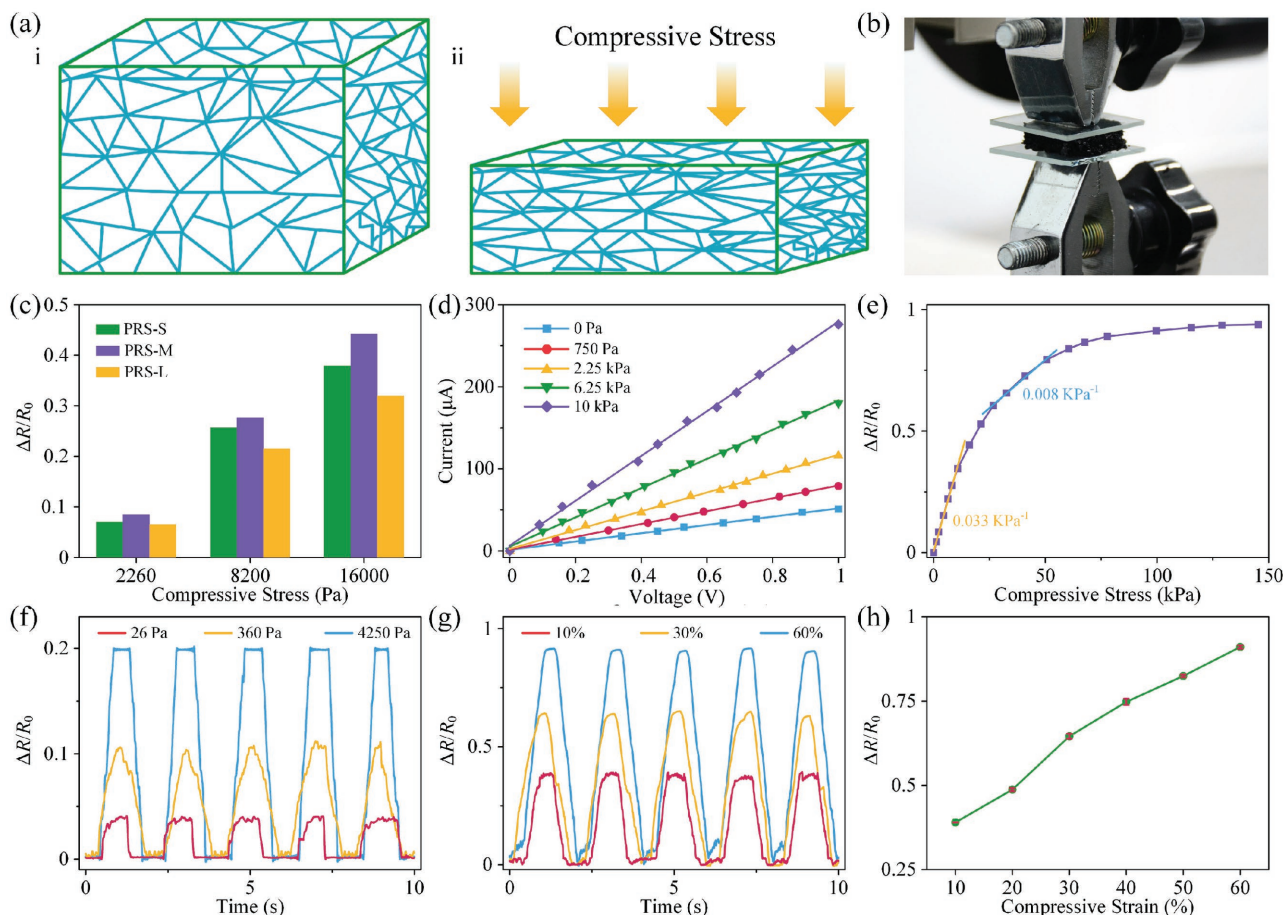


Figure 3. Characterization of the resistance response of PRS. a) Stress-sensing models of as-prepared PRS, showing the contact area variation of conductive scaffold with compressive deformation. b) Piezoresistance measurements of the PRS with the push-pull gauge. c) Resistance responses of different PRSs under the different compressive stress. d) Current–voltage (I – V) curves of PRS under different compressive stress. e) Stress–response curves for PRS, the sensitivity of which attains 0.03 kPa^{-1} in low stress range. f) Resistance responses of repeated compressing and releasing cycles with different stress. The minimum stress is as low as 26 Pa. g) Resistance responses of repeatedly compressing tests of PRS at different strains. The maximum strain is as high as 60%. h) Resistance response variation with the different compressive strains.

connecting wire in the circuit (Figure S4, Supporting Information). As the applied stress is compressed and released, the LED subsequently becomes bright and dim, respectively. In addition, the sensitivity of the PRS is also evaluated and the plot of $\Delta R/R_0$ versus applied compressive stress is shown in Figure 3e. The stress sensitivity of S can be defined as the slope of the curves:

$$S = \delta(\Delta R/R_0) / \delta P \quad (1)$$

where P represents the compressive stress. The $\Delta R/R_0$ shows a linear increase against increasing compressive stress in the first 0–15 kPa range, exhibiting a good sensitivity of 0.03 kPa^{-1} . After the fully contact of CNT–PDMS sponge conductive scaffold, the sensitivity decreases to 0.008 kPa^{-1} as the applied compressive stress gets higher. Notably, the initially linear increasing region corresponds to the Regions I and II (Figure 2h) and has the same dividing point with the stress–strain measurements, which is discussed in detail (Figure S5, Supporting Information).

As for overall measurements, the resistance responses to repeated compressing and releasing cycles are illustrated in Figure 3f. Low stress (26 Pa) could be detected by PRS and reliable resistance responses are observed under different compressive stress, which is comparable to other minimum detectable pressure sensors.^[18] As the compressive stress increases to 4.2 kPa, the intensity of signal becomes higher and more stable. These resistance responses of PRS to small compressive stress show potential applications in detecting tiny motions, such as speech and airflow. Additionally, at the large repeated strains, a serial of resistance responses could be obtained (Figure 3g). For different compressive strains from 10% to 60%, higher strain will bring in larger resistance response intensity. As shown in Figure 3h, the resistance response is quite stable under the same strain condition. Such distinguishing response signals in large strains make the PRS capable of differentiating and reflecting large-scale human movements, such as breathing and walking.

Table S1 in the Supporting Information compares the results of our sensing performance and other reported researches.^[18,23,26,46,47] Along with the enhanced sensitivity,

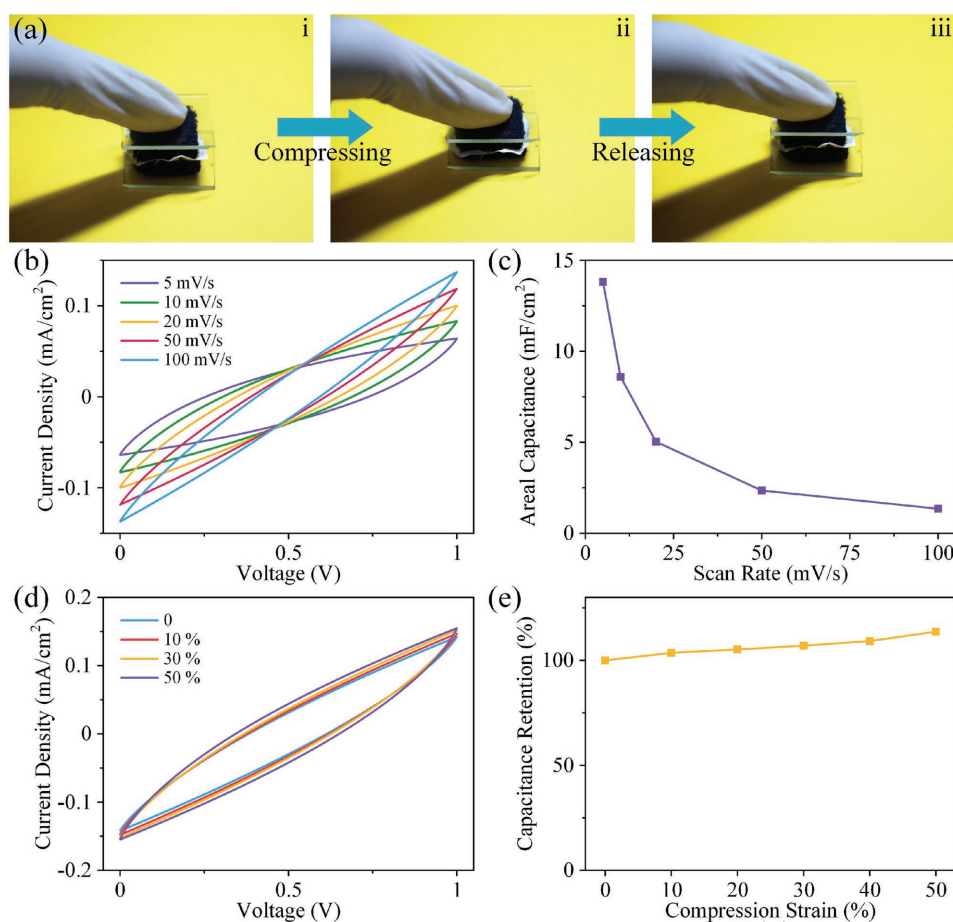


Figure 4. a) Digital photographs showing compression-tolerant ability with the compressing and releasing process of the CSC device. Electrochemical behavior of the CSC. b) CV curves at different scan rates. c) Calculated areal capacitance as a function of voltage scan rate. d) CV curves and e) capacitance retention of the CSC under different compressive strains.

other performances of our sensor have not been influenced, such as the fast response and stable compressing–releasing cycles. For the response capability of the PRS, it exhibits a response time of 100 ms (release-time) and 300 ms (rise-time) (Figure S6, Supporting Information), which could be utilized as a real-time health monitor of wearable devices. The cycling stability of our prepared PRS is also measured as shown in Figure S7 in the Supporting Information. The resistance response with applied strain (20%) could maintain stable after 2000 compressing–releasing cycles, implying long working stability of the PRS. As a result, such CNT–PDMS sponge shows great candidates as sensitive and stable PRS for various applications, such as wearable monitor devices and electronic artificial skin.

2.3. Electrochemical Performance of CSC

On the other hand, based on the CNT–PDMS sponge with excellent hydrophilicity and mechanical stability, we fabricate the solid-state CSC with polyvinyl alcohol/phosphoric acid (PVA/H₃PO₄) gel electrolyte and separator membrane at the volume of 1.8 × 1.8 × 1 cm³. After a compressing–releasing cycle, the CSC could return to the origin state, suggesting the

volume of CSC could be totally recovered without plastic deformations (Figure 4a). To further evaluate the electrochemical performance, the CSC is carefully characterized through cyclic voltammetry (CV), galvanostatic charge–discharge (GCD), and cycling stability measurements via electrochemical workstation. First, in the CV curves of the CSC at a stable potential window between 0 and 1 V, they retain quasi-rectangular shapes and are approximately symmetrical about the zero-current line, indicating the fast charging–discharging rate and an ideal electrical double layer behavior (Figure 4b). Under the scan rates from 5 to 100 mV s^{−1}, the volumetric capacitance (C_V) is calculated by the following equations:

$$C_V = \frac{Q}{V \cdot \Delta V} = \frac{1}{k \cdot V \cdot \Delta V} \int_{V_1}^{V_2} I(V) dV \quad (2)$$

where $I(V)$ is the charge–discharge current function, k is the scan rate, V is the volume of the CSC and ΔV is the potential window during the discharge process, where V_1 and V_2 are maximum and minimum voltage values, respectively. The maximum volumetric capacitance is 13.82 mF cm^{−3} at scan rate of 5 mV s^{−1}, and this CSC could withstand the charging–discharging process without significant degradation

in volumetric capacitance even at high scan rates (Figure 4c), thus demonstrating a stable electrochemical performance. In addition, GCD curves are also measured, the charging–discharging currents of which are from 1 to 4 mA (Figure S8, Supporting Information). The charging profile of the device is dependent on the applied current and symmetrical with their corresponding discharging counterparts. Meanwhile, the CSC also shows excellent stability under CV test at a scan rate of 100 mV s⁻¹ for 3000 cycles, and the cycling performance is shown in Figure S9 in the Supporting Information. It demonstrates that the capacitance of the device increases at the beginning due to the electrode self-activation process. Then it degrades gradually and remains about 98.44% after 3000 cycles compared with the first cycle. Therefore, the CSC owns stable and excellent electrochemical performance and satisfies the needs of low-power energy supply.

In addition, when the CSC is applied with different compressive strains, no significant change is observed in the CV curves even under 50% applied strain (Figure 4d). Such desirable electrochemical stability under different compressive strains could be attributed to the stable electrical double layer configuration. The capacitance retention of CSC is also calculated through Equation (2) and discussed in Figure 4e. The performance of the CSC experiences slightly improvement with the increasing compressive strains due to the shorten length between CNT–PDMS sponge conductive scaffold and improvement of the rate capability. Direct comparison between this work and several of the compressible supercapacitors developed by pioneers in field shows that our CSC owns desirable performance to meet the demands of various applications (Table S2, Supporting Information).^[34,48,49]

2.4. Applications of Compressible Systems

To accommodate the practical applications with complex conditions, we assemble the highly compressible system integrated the PRS and the CSC. As the little signal of PRS may increase the testing difficulties powered by a single CSC, several CSCs could be interconnected in serial on one chip and an enhanced potential range of the system could be provided. Detailed description of the compressible system is shown in Figure S10 in the Supporting Information, which proves that such highly compressible integrated system consisting of the CSC and PRS performs stably to power and modulate the low-power electronic devices even under compressive strains.

Considering the fact that this CNT–PDMS sponge has the capabilities in monitoring small-scale human motions, the wearable and sensitive PRS could be attached to the throat of a healthy person directly and the serial CSC unit could be placed on the coat pocket as the steady power supply (Figure 5a). To meet the demands of the actual application, the whole PRS device is packaged with two polyimide tapes to response the stress variations reliably. The detailed fabrication illustration is depicted in the Figure S11 in the Supporting Information. When the CSC unit is charged to 2 V, resistance variation (R_X) could be calculated through the voltage signal of the constant resistance according to the circuit diagram (inset of Figure 5a) as follows:

$$R_X = \left(\frac{V_C}{V_0} - 1 \right) \cdot R_P \quad (3)$$

where R_P represents the constant resistance, V_C , and V_0 represent the voltage of the CSC and the voltage signal of the R_P , respectively. The PRS is utilized to monitor the muscle movements near the throat noninvasively. The working principle of human motion monitoring is depicted in the Figure S12 in the Supporting Information. When the speaker pronounced different polite expressions, the PRS powered by CSC could distinguish different signals of muscle motions with high sensitivity and good repeatability, such as “Hi,” “Hello,” and “Bye.” As shown in Figure 5b, apparently different resistance response could be recorded and nearly same waveforms are stably provided, which shows the promising potentials in robotics speech recognition. Additionally, when a person is drinking water, the motions around the throat produce distinct resistance responses as shown in Figure 5c and yawning could also provide resistance response which owns both positive and negative due to the motion characteristic as shown in Figure S13 in the Supporting Information. These different signal waveforms of the compressible system enable us to differentiate the various muscle movements of the human esophagus (drinking) and trachea (yawning), which plays an important role in distinguishing human’s physiological activities and working as real-time health monitor.

With the high compressibility and great piezoresistance performance, such compressible system is qualified to perform reliably in large-scale movement monitoring as well. Figure 5d shows the wearable and sensitive packaged PRS could be attached to the inside of crus directly and the serial CSC unit could be placed on the shorts pocket to monitor human movements. The player is conducted to perform different movements, such as walking, jogging, and running. It can be observed that PRS exerts different responsive signals to different motions of the crus (Figure 5e). In detail, walking motion and running motion represent both small-scale and large-scale bending process of the crus and PRS experiences correspondingly small and large current response, respectively. As a result, the larger the motion range is, the higher the current response reaches. These results confirm the satisfactory capability of PRS to distinguish different-scale movements.

Furthermore, integrated with the normal waistband, the compressible system could be directly tied among the human body as the breathing monitor device shown in Figure 5f. It is known that diaphragmatic breathing is the most natural way, and the monitoring information of the diaphragm is very important for diagnosis of disease, medical treatment, and postoperative care. On inspiration process, the PRS is gradually compressed, accompanied with the increase of the circuit current. While on expiration process, the compressed PRS releases to its original condition, leading to the recovery of the circuit current. As shown in Figure 5g, this compressible system could monitor the person recovery-breathing rate after the exercise. When a healthy subject is running for ten minutes, the breathing rate is increasing to 75 times per minute, then with the body relaxing, the breathing rate gets

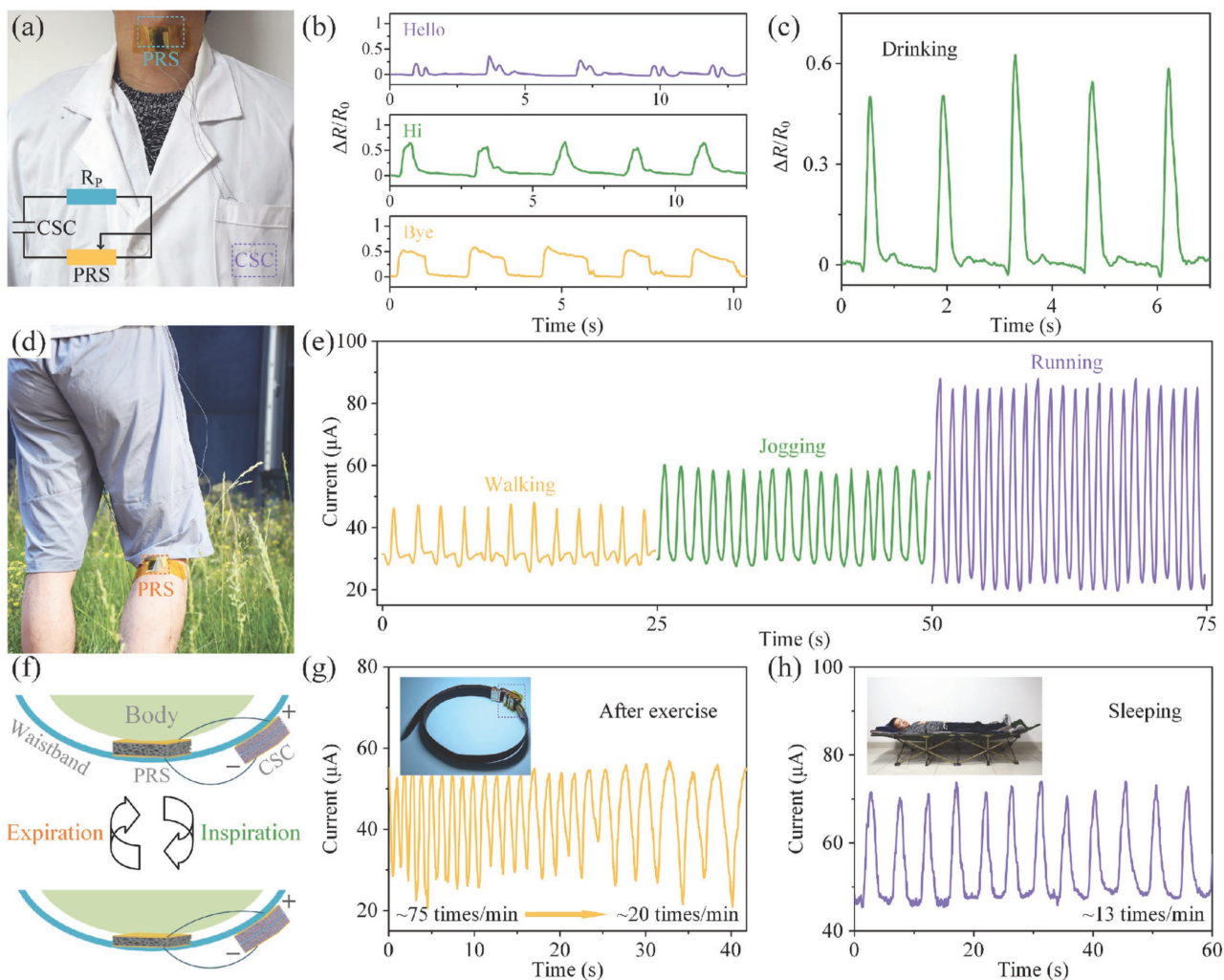


Figure 5. a) Photograph of the compressible system with PRS attached to the neck and CSC placed onto the coat pocket to monitor human motions. Inset photograph shows the circuit diagram of the resistance response recording. Recorded resistance response versus time during b) the pronunciation of polite expressions and c) drinking. d) Photograph of the compressible system with PRS attached to the inside of crus and CSC placed onto the shorts pocket to monitor human movements. e) Recorded current–time curve of the compressible system as the human is walking, jogging, and running, respectively. f) Schematic illustration for human breath monitoring by using compressible system. Recorded current–time curve of the compressible system as the human breathing monitor g) after exercise and h) during sleeping condition. Inset photograph shows the compressible system could be attached on a wristband.

smooth and decreases to 20 times per minute. The recovery process could be recorded to further analysis of cardiac and pulmonary function. In addition, such system could also monitor the sleeping conditions, during which time, the repeated compressing–releasing processes give typical current variations as shown in Figure 5h. The person with a breathing periodicity of 13 times per minute could be obtained from the recorded signal, showing the possibility of the compressible system in further applications includes disease surveillance and human–machine interfaces.

3. Conclusions

In summary, a highly compressible integrated supercapacitor–piezoresistance-sensor system based on a generally wearable CNT–PDMS sponge is proposed. The sponge-like

PDMS scaffold is synthesized using a template of cost-effective material of sugar. Through drop-drying process of CNT ink dispersion, porous architecture CNT–PDMS sponge is developed with high conductivity and mechanical property. On one hand, the CNT–PDMS sponge owns piezoresistance characteristic with high sensitivity and capability of monitoring various compressive stresses. Notably, the PRS made of CNT–PDMS sponge could detect low compressive stress (26 Pa), own good sensitivity (0.03 kPa^{-1}), and response reliable signals under repeated compressive stress. On the other hand, with hydrophilicity and electrochemical performance, it could be the ideal material for solid-state CSC. Assembled with the CNT–PDMS sponge electrode and PVA/ H_3PO_4 gel electrolyte, the CSC achieves a maximum volumetric capacitance of 13.82 mF cm^{-3} , and stable electrochemical performance under different compressive strains. Composed with the PRS and the CSC, such highly compressible integrated

system performs stably to power and modulate the low-power electronic devices. Furthermore, taking advantages of the high sensitivity of PRS, various human motions (such as pronouncing, drinking, breathing, etc.) could be recorded through the circuit diagram powered by the CSC regardless of the working conditions. Therefore, with the general CNT–PDMS sponge attached to the epidermal skin or waistband, this highly compressible integrated system consisting of PRS and CSC shows promising potentials in distinguishing human's physiological motions and real-time health monitor.

4. Experimental Section

Fabrication of PDMS Sponges: Compressible PDMS sponges were prepared using a sugar cube as the template. Sugar cubes could be purchased such as Taikoo cube sugar with an area of $2 \times 2 \times 1 \text{ cm}^3$ (Taikoo Sugar Co.). First, the elastomer and cross-linker of commercial PDMS (Sylgard 184, Dow Corning Co.) were mixed with a quantity ratio of 10:1. After the air bubbles trapped during the agitation of mixture were removed under the gentle vacuum conditions, the cube sugars were placed into the PDMS mixture where PDMS mixture could be infiltrated into the porous structure by vacuum pumping process and capillary force. The size of the pores and porosity were determined by the granularity of sugar. The samples were then cured at atmospheric conditions for 30 min at 120 °C, and the sugars were dissolved in the hot water under sonication bath for 1 h. Finally, the PDMS sponges were prepared after drying the samples overnight with different thickness.

Fabrication of CNT–PDMS Sponges: The highly compressible CNT–PDMS sponges were fabricated simply by drop-drying method. CNT ink dispersion was prepared by dispersing CNTs (200 mg, Boyu Co., China) and 200 mg sodium dodecylbenzenesulfonate as the surfactant in 200 mL of deionized water. Bath sonicated for 4 h to disperse CNTs evenly, the CNT ink dispersion was subsequently dropped onto the surface of PDMS sponge and the resistance of samples was relevant to the dropping cycles. The CNT–PDMS sponges were rinsed several times using deionized water to remove the surfactant. Finally, the CNTs were evenly coated onto the scaffold surface of the PDMS sponge, leading to a CNT density of 0.2 g cm^{-3} . Afterward, assembled with two PET/ITO substrates onto the top and bottom surfaces of as-obtained CNT–PDMS sponge as electrodes, the PRS could be prepared and recorded the resistance responses under corresponding compressing.

Fabrication of the Compressible Supercapacitor: The solid-state CSC devices were assembled from two pieces of CNT–PDMS sponges ($1.8 \times 1.8 \times 0.5 \text{ cm}^3$) with a separator and PVA/ H_3PO_4 gel as the solid electrolyte. Gel electrolyte was prepared by mixing 6 g H_3PO_4 with 60 mL deionized water and 6 g PVA powder. The mixture was heated up to 85 °C under vigorous stirring until the solution becomes clear. Typically, two pieces of CNT–PDMS sponge were placed onto two PET/ITO substrates ($2 \times 2 \text{ cm}^2$) and PVA/ H_3PO_4 gel electrolyte was dropped onto the surfaces until the CNT–PDMS sponge was saturated. Then all parts were assembled into symmetrical supercapacitor with a cellulose separator (TF44, NKK Co., Japan). Finally, the compressible device was left in the fume hood at room temperature to fully vaporize the excess water.

Characterization: The structure and morphology of the materials were characterized using SEM (Quanta 600F, FEI Co.). The mechanical measurements of the samples were carried out using a push–pull gauge (Handpi Co.). Additionally, the voltage of the PRS was amplified by a SR560 low-noise voltage amplifier from Stanford Research Systems and measured via a digital oscilloscope (Agilent DSO-X 2014A). For the electrochemical performance of the CSC, a CHI660 electrochemical workstation (Chenghua Co., China) was utilized by using CV and GCD techniques with a two-electrode configuration. Dynamic water contact angle measurements were recorded by the contact angle measurement system (OCA 30, Data Physics Instruments GmbH).

Supporting Information

Supporting Information is available from the Wiley Online Library or from the author.

Acknowledgements

This work was supported by National Key R&D Project from Minister of Science and Technology, China (2016YFA0202701), the National Natural Science Foundation of China (Grant Nos. 61674004, 61176103, and 91323304), and the Beijing Natural Science Foundation of China (Grant No. 4141002).

Conflict of Interest

The authors declare no conflict of interest.

- [1] H. Hu, Z. Zhao, W. Wan, Y. Gogotsi, J. Qiu, *Adv. Mater.* **2013**, *25*, 2219.
- [2] L. Liu, Y. Yu, C. Yan, K. Li, Z. Zheng, *Nat. Commun.* **2015**, *6*, 7260.
- [3] Y. Song, X. Cheng, H. Chen, J. Huang, X. Chen, M. Han, Z. Su, B. Meng, Z. Song, H. Zhang, *J. Mater. Chem. A* **2016**, *4*, 14298.
- [4] Y. Huang, S. V. Kershaw, Z. Wang, Z. Pei, J. Liu, Y. Huang, H. Li, M. Zhu, A. L. Rogach, C. Zhi, *Small* **2016**, *12*, 3393.
- [5] N. Wu, X. Cheng, Q. Zhong, J. Zhong, W. Li, B. Wang, B. Hu, J. Zhou, *Adv. Funct. Mater.* **2015**, *25*, 4788.
- [6] Y. Jie, H. Zhu, X. Cao, Y. Zhang, N. Wang, L. Zhang, Z. L. Wang, *ACS Nano* **2016**, *10*, 10366.
- [7] Y. Yu, J. Zeng, C. Chen, Z. Xie, R. Guo, Z. Liu, X. Zhou, Y. Yang, Z. Zheng, *Adv. Mater.* **2014**, *26*, 810.
- [8] S. J. Kim, J. H. We, B. J. Cho, *Energy Environ. Sci.* **2014**, *7*, 1959.
- [9] J. Ren, Y. Zhang, W. Bai, X. Chen, Z. Zhang, X. Fang, W. Wang, Y. Wang, H. Peng, *Angew. Chem.* **2014**, *126*, 7998.
- [10] K. Guo, N. Yu, Z. Hou, L. Hu, Y. Ma, H. Li, T. Zhai, *J. Mater. Chem. A* **2017**, *5*, 16.
- [11] P. Bai, G. Zhu, Q. Jing, J. Yang, J. Chen, Y. Su, J. Ma, G. Zhang, Z. L. Wang, *Adv. Funct. Mater.* **2014**, *24*, 5807.
- [12] H. Park, Y. R. Jeong, J. Yun, S. Y. Hong, S. Jin, S.-J. Lee, G. Zi, J. S. Ha, *ACS Nano* **2015**, *9*, 9974.
- [13] K. Shi, X. Yang, E. D. Cranston, I. Zhitomirsky, *Adv. Funct. Mater.* **2016**, *26*, 6437.

- [14] B.-U. Hwang, J.-H. Lee, T. Q. Trung, E. Roh, D.-I. Kim, S.-W. Kim, N.-E. Lee, *ACS Nano* **2015**, *9*, 8801.
- [15] X. Zhang, M. Su, J. Brugger, B. Kim, *Nano Energy* **2017**, *33*, 393.
- [16] S. Gong, W. Schwalb, Y. Wang, Y. Chen, Y. Tang, J. Si, B. Shirinzadeh, W. Cheng, *Nat. Commun.* **2014**, *5*, 3132.
- [17] S. Jung, J. H. Kim, J. Kim, S. Choi, J. Lee, I. Park, T. Hyeon, D. H. Kim, *Adv. Mater.* **2014**, *26*, 4825.
- [18] X. Wu, Y. Han, X. Zhang, Z. Zhou, C. Lu, *Adv. Funct. Mater.* **2016**, *26*, 6246.
- [19] Y. Li, Y. A. Samad, K. Liao, *J. Mater. Chem. A* **2015**, *3*, 2181.
- [20] V. T. Dau, C. D. Tran, T. T. Bui, V. D. Nguyen, T. X. Dinh, *RSC Adv.* **2016**, *6*, 106090.
- [21] V. T. Dau, T. Yamada, D. T. Dao, B. T. Tung, K. Hata, S. Sugiyama, *Microelectron. J.* **2010**, *41*, 860.
- [22] J.-W. Han, B. Kim, J. Li, M. Meyyappan, *Appl. Phys. Lett.* **2013**, *102*, 051903.
- [23] H. Chen, Z. Su, Y. Song, X. Cheng, X. Chen, B. Meng, Z. Song, D. Chen, H. Zhang, *Adv. Funct. Mater.* **2016**, *27*, 1604434.
- [24] X. Gui, A. Cao, J. Wei, H. Li, Y. Jia, Z. Li, L. Fan, K. Wang, H. Zhu, D. Wu, *ACS Nano* **2010**, *4*, 2320.
- [25] R. Rahimi, M. Ochoa, W. Yu, B. Ziaie, *ACS Appl. Mater. Interfaces* **2015**, *7*, 4463.
- [26] H. B. Yao, J. Ge, C. F. Wang, X. Wang, W. Hu, Z. J. Zheng, Y. Ni, S. H. Yu, *Adv. Mater.* **2013**, *25*, 6692.
- [27] S. Chun, A. Hong, Y. Choi, C. Ha, W. Park, *Nanoscale* **2016**, *8*, 9185.
- [28] C. Zhu, P. Kopold, P. A. van Aken, J. Maier, Y. Yu, *Adv. Mater.* **2016**, *28*, 2409.
- [29] Y. Song, X. Cheng, H. Chen, M. Han, X. Chen, J. Huang, Z. Su, H. Zhang, *Micro Nano Lett.* **2016**, *11*, 586.
- [30] Z. Lin, Z. Zeng, X. Gui, Z. Tang, M. Zou, A. Cao, *Adv. Energy Mater.* **2016**, *6*, 1600554.
- [31] Y. Song, X. Chen, J. Zhang, X. Cheng, H. Zhang, *J. Microelectromech. Syst.* **2017**, *PP*, 1.
- [32] P. Simon, Y. Gogotsi, *Nat. Mater.* **2008**, *7*, 845.
- [33] C. Shen, X. Wang, S. Li, W. Zhang, F. Kang, *J. Power Sources* **2013**, *234*, 302.
- [34] K. Xiao, L. X. Ding, G. Liu, H. Chen, S. Wang, H. Wang, *Adv. Mater.* **2016**, *28*, 5997.
- [35] Z. Niu, W. Zhou, X. Chen, J. Chen, S. Xie, *Adv. Mater.* **2015**, *27*, 6002.
- [36] Y. Zhao, J. Liu, Y. Hu, H. Cheng, C. Hu, C. Jiang, L. Jiang, A. Cao, L. Qu, *Adv. Mater.* **2013**, *25*, 591.
- [37] P. Li, C. Kong, Y. Shang, E. Shi, Y. Yu, W. Qian, F. Wei, J. Wei, K. Wang, H. Zhu, *Nanoscale* **2013**, *5*, 8472.
- [38] P. Li, E. Shi, Y. Yang, Y. Shang, Q. Peng, S. Wu, J. Wei, K. Wang, H. Zhu, Q. Yuan, *Nano Res.* **2014**, *7*, 209.
- [39] Y. Qin, J. Yuan, J. Li, D. Chen, Y. Kong, F. Chu, Y. Tao, M. Liu, *Adv. Mater.* **2015**, *27*, 5171.
- [40] J. Zhao, H. Lai, Z. Lyu, Y. Jiang, K. Xie, X. Wang, Q. Wu, L. Yang, Z. Jin, Y. Ma, *Adv. Mater.* **2015**, *27*, 3541.
- [41] W. Liu, Z. Chen, G. Zhou, Y. Sun, H. R. Lee, C. Liu, H. Yao, Z. Bao, Y. Cui, *Adv. Mater.* **2016**, *28*, 3578.
- [42] H. Li, Y. Ding, H. Ha, Y. Shi, L. Peng, X. Zhang, C. Ellison, G. Yu, *Adv. Mater.* **2017**, *29*, 1700898.
- [43] S. Liang, Y. Li, J. Yang, J. Zhang, C. He, Y. Liu, X. Zhou, *Adv. Mater. Technol.* **2016**, *1*, 1600117.
- [44] D. Kim, S. Park, S. Jeon, M. Seol, Y. Choi, *Adv. Electron. Mater.* **2016**, *2*, 1500331.
- [45] W. McCall, K. Kim, C. Heath, G. Pierre, D. Sirbully, *ACS Appl. Mater. Interfaces* **2014**, *6*, 19504.
- [46] J. Kuang, Z. Dai, L. Liu, Z. Yang, M. Jin, Z. Zhang, *Nanoscale* **2015**, *7*, 9252.
- [47] J. Nassar, M. Cordero, A. Kutbee, M. Karimi, G. Sevilla, A. Hussain, A. Shamim, M. Hussain, *Adv. Mater. Technol.* **2016**, *1*, 1600004.
- [48] M. Sevilla, A. B. Fuertes, *ACS Nano* **2014**, *8*, 5069.
- [49] J. Wang, B. Ding, Y. Xu, L. Shen, H. Dou, X. Zhang, *ACS Appl. Mater. Interfaces* **2015**, *7*, 22284.

Received: June 20, 2017
Published online: August 8, 2017